A high-resolution optical measurement system for rapid acquisition of radiation flux density maps

Martin Thelen, Christian Raeder, Christian Willsch, and Gerd Dibowski

Citation: AIP Conference Proceedings **1850**, 150005 (2017); doi: 10.1063/1.4984534
View online: http://dx.doi.org/10.1063/1.4984534
View Table of Contents: http://aip.scitation.org/toc/apc/1850/1
Published by the American Institute of Physics

A High-Resolution Optical Measurement System for Rapid Acquisition of Radiation Flux Density Maps

Martin Thelen[1, a)], Christian Raeder[1, b)], Christian Willsch[1] and Gerd Dibowski[1]

[1]*German Aerospace Center*
Institute of Solar Research, Facilities and Solar Materials, Linder Höhe, 51147 Koeln, Germany

[a)]Corresponding author: martin.thelen@dlr.de
[b)]christian.raeder@dlr.de

Abstract. To identify the power and flux density of concentrated solar radiation the Institute of Solar Research at the German Aerospace Center (DLR – Deutsches Zentrum für Luft- und Raumfahrt e. V.) has used the camera-based measurement system FATMES (Flux and Temperature Measurement System) since 1995. The disadvantages of low resolution, difficult handling and poor computing power required a revision of the existing measurement system. The measurement system FMAS (Flux Mapping Acquisition system) is equipped with state-of-the-art-hardware, is compatible with computers off-the-shelf and is programmed in LabView. The expenditure of time for an image evaluation is reduced by the factor 60 compared to FATMES. The new measurement system is no longer associated with the facilities Solar Furnace and High Flux Solar Simulator at the DLR in Cologne but is also applicable as a mobile system. The data and the algorithms are transparent throughout the complete process. The measurement accuracy of FMAS is determined to at most ± 3 % until now. The error of measurement of FATMES is at least 2 % higher according to the conducted comparison tests.

HARDWARE

A common measurement setup of an optical flux measurement system is shown in Fig. 1. A camera acquires an image of an irradiated and water-cooled target. The targets surface is coated with a diffuse reflecting aluminum oxide ceramic to obtain lambertian properties, thus enabling the operator to position the camera under a certain angle with respect to the target plane. *FMAS* processes 8 bit images with 256 gray values from 0 (black) to 255 (white). The camera with GigE interface is combined with an anti-shading lens. Due to the highly-intense radiation a set of neutral-density filters is used.

SolarPACES 2016
AIP Conf. Proc. 1850, 150005-1–150005-11; doi: 10.1063/1.4984534
Published by AIP Publishing. 978-0-7354-1522-5/$30.00

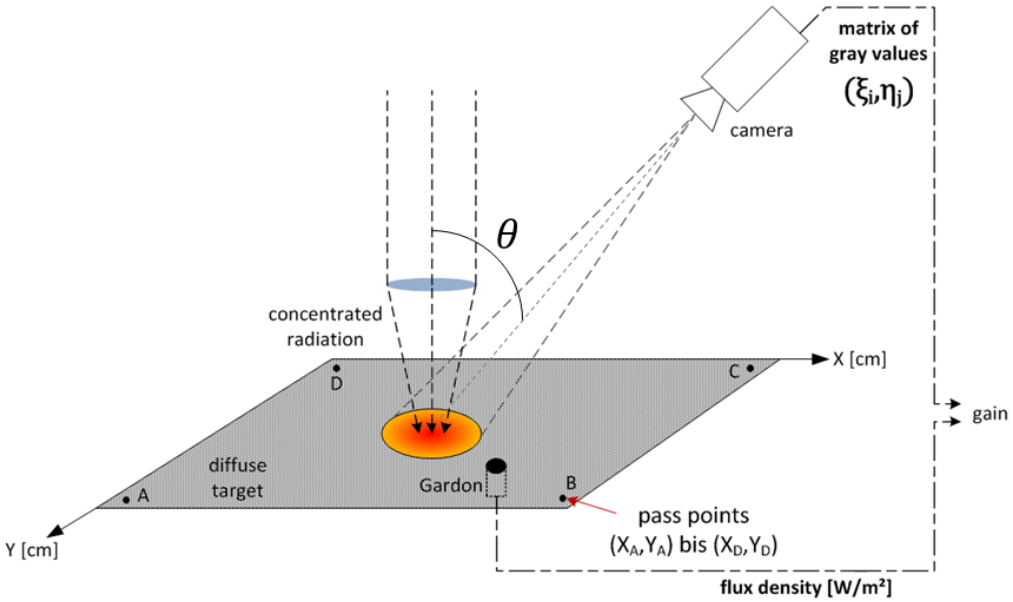

FIGURE 1. Measurement setup

In order to scale the camera's gray value matrix the flux density emerging from at least one pixel has to be known. Figure 1 sketches a Gardon radiometer whose sensitive foil is placed in the same plane as the Lambertian surface. Its position has to be within the rectangle surrounded by the pass points on the target that are obligatory for the later image rectification. The flux density is alternatively measured by a Kendall radiometer or a SUNCATCH calorimeter. These types have a higher response time due to their cavity structures but show lower measurement errors. The accuracy of Gardon radiometers is specified to ± 0.7 % [1], while Kendall radiometers display an error of ± 0.3 % [2] and SUNCATCH calorimeters read ± 0.5 % [3].

Gardon radiometers and the SUNCATCH calorimeter at the DLR Institute for Solar Research are calibrated using the sensor *Kendall Mk IX* to ensure the above measurement accuracies [4]. The Kendall radiometer has the ability to be calibrated internally. The cavity has a heating wire attached to its rear side. By energizing the heating wire a voltage at the cavity's thermopile results. The calibration factor K_{korr} of the Kendall radiometer is calculated as shown in equation (1).

$$K_{korr}\left[\frac{W}{m^2 \cdot V}\right] = \frac{U_H[V] \cdot I_H[A]}{U_{Th}[V] - U_0[V]} \cdot C_F\left[\frac{1}{m^2}\right] \tag{1}$$

The offset voltage U0 is less than 10 µV. UH and IH describe the voltage and the current applied to the heating wire. UTh is the thermopile voltage which is in fact the measurement signal. The correction factor $C_F = 334100\ m^{-2}$ is given by the manufacturer and results from equation (2).

$$C_F\left[\frac{1}{m^2}\right] = \frac{1}{A \cdot a \cdot R} \tag{2}$$

The aperture of the Kendall Mk IX is $A = 0.02966 \cdot 10^{-4}\ m^2$ (diameter 1.9 mm), $a = 0.992$ indicates the absorptance of the cavity's dull black coating and $R = 1.003$ considers the measurement inaccuracy of ± 0.3 %. By approximation, there is a linear relationship between the calibration factor and the thermopile voltage. Both the gradient and the intercept depend on the temperature of the cooling water T_k (see Fig. 2). Equation (3) shows the linear regression for calculating the flux as a function of the thermopile voltage and the cooling water temperature.

$$E = U_{Th} \cdot K_{korr}(U_{Th}, T_k) = U_{Th} \cdot [m(T_k) \cdot U_{Th} + b(T_k)] \tag{3}$$

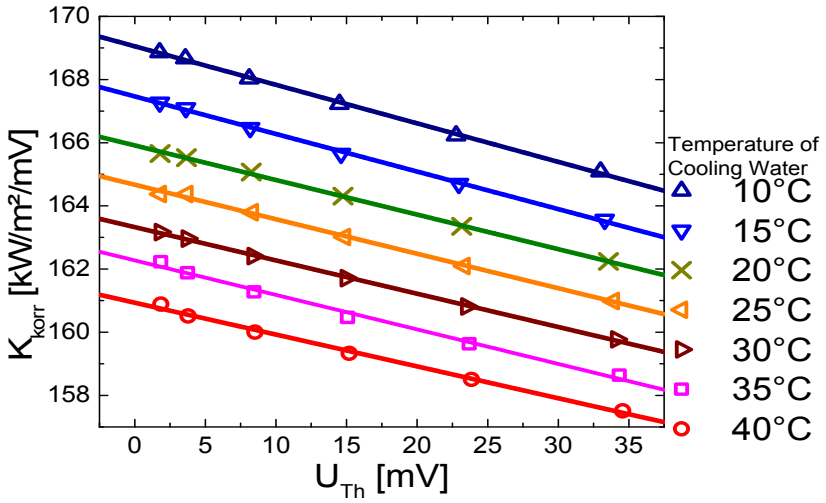

FIGURE 2. Temperature-dependent calibration of the Kendall Mk IX

The Gardon radiometer response time is less than one second. Intercomparison campaigns on a regular basis ([5], [6]) combine the accuracy of the Kendall type radiometer with the fast response time of a Gardon type radiometer.

IMAGE PROCESSING

Figure 3 shows a flow chart illustrating the sequence of subtasks used to calculate a flux map from the camera's gray value distribution and the sensor output in absolute units (W/m²) at the location of the radiometer in the picture. The underlying photo containing the gray value distribution does not include the sensor surface. After reading the signal the Lambertian target is moved (see Fig. 6).

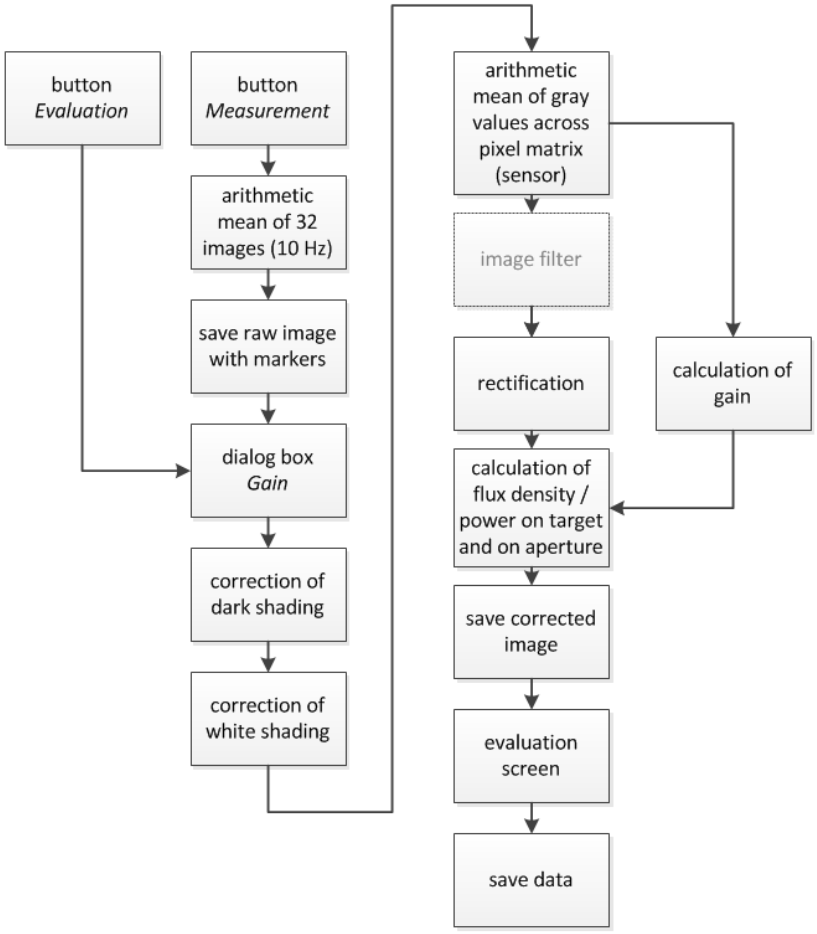

FIGURE 3. Image correction and processing algorithms

FMAS is both designed to take a dark current image of an irradiated target and evaluate an existing gray value matrix from a Bitmap file. By clicking the "Measurement" button the camera is triggered to take 32 equidistant images within 3.2 seconds. The arithmetic mean of those pictures is calculated and stored as raw image. An additional text file is used to save the position information of the five markers (pass points and sensor). The user is then asked to specify the flux from the radiometer signal which is buffered for later use. The next step of the evaluation sequence is the correction of two influential and inherent camera errors. First, the known dark image $[D]_{ij}$ is subtracted from the raw picture matrix $[I]_{ij}$ to achieve the dark shading corrected image $[I]_{ij}^{D}$ (see equation (4)).

$$[I]_{ij}^{D} = [I]_{ij} - [D]_{ij} \tag{4}$$

This image is utilized to compensate the white shading due to inhomogeneous illumination of the camera's CCD chip. The resulting image $[I]_{ij}^{res}$ is calculated by equation (5). A set of aperture-dependent shading images $[S]_{ij}^{D}$, taken with means of an integrating sphere, of the camera's objective is stored on the hard disk drive. The Quotient with the mean gray value $\bar{S}$ of the shading image is a weighting coefficient describing the differences in brightness of the shading image.

$$[I]_{ij}^{res} = [I]_{ij}^{D} \cdot \frac{\bar{S}}{[S]_{ij}^{D}} \tag{5}$$

For a clear delimitation of the illuminated area on the target, *FMAS* conducts a local contrast enhancement using the picture matrix $[I]_{ij}^{res}$ after the dark and white shading compensation.

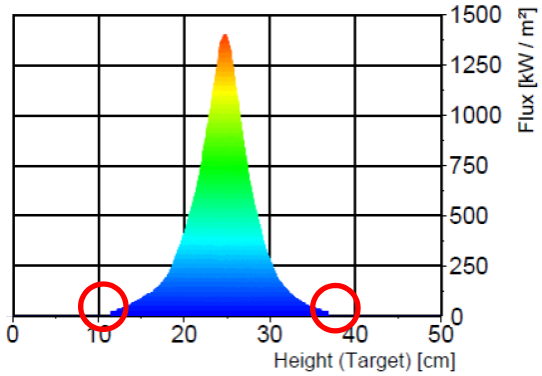

FIGURE 4. Edges of flux density distribution

Figure 4 illustrates the effect of the local contrast enhancement at the edge of the beam profile. To achieve a clear border, each pixel of the image that has a gray value lower than 4 is set to zero.

The described gray value operations are followed by an image rectification. From this point, the pixel values are scaled and appear as flux density values. The scaling factor "Gain" is calculated by the division of the buffered sensor signal and the mean value of all gray values within the marked rectangle at the sensor's position (see equation (6)). For strong flux gradients the Kendall Mk IX can be used to reduce the error of this calculation because its aperture area is about 180 times smaller than that of a 1" Gardon gauge. The rectangle surrounding the sensitive area of the Kendall Mk IX includes fewer pixels. Thus, local flux gradients are detected more accurate.

$$Gain = \frac{E_{sensor\ pixels}}{\overline{GW}_{sensor\ pixels}} \tag{6}$$

To correct the projective error that occurs due to a transversal viewing angle of the camera onto the irradiated target, the image rectification has to be conducted using the four pass point markers. The linear equation system (11) calculates the 8 unknown parameters a_1 to c_2 by circumscribing equations (7) and (8).

$$X = \frac{a_1\xi + a_2\eta + a_3}{c_1\xi + c_2\eta + 1} \tag{7}$$

$$Y = \frac{b_1\xi + b_2\eta + b_3}{c_1\xi + c_2\eta + 1} \tag{8}$$

ξ, η mean the pixel coordinates and X, Y are the corresponding real-world coordinates of the pass points A to D (see Figure 1). The expanded notation is shown in the equations (9) and (10).

$$X = \xi a_1 + \eta a_2 + a_3 - X\xi c_1 - X\eta c_2 \tag{9}$$

$$Y = \xi b_1 + \eta b_2 + b_3 - Y\xi c_1 - Y\eta c_2 \tag{10}$$

The linear equation system (11) eventually can be quoted as follows:

$$\begin{pmatrix} \xi_A & \eta_A & 1 & 0 & 0 & 0 & -X_A\xi_A & -X_A\eta_A \\ 0 & 0 & 0 & \xi_A & \eta_A & 1 & -Y_A\xi_A & -Y_A\eta_A \\ \xi_B & \eta_B & 1 & 0 & 0 & 0 & -X_B\xi_B & -X_B\eta_B \\ 0 & 0 & 0 & \xi_B & \eta_B & 1 & -Y_B\xi_B & -Y_B\eta_B \\ \xi_C & \eta_C & 1 & 0 & 0 & 0 & -X_C\xi_C & -X_C\eta_C \\ 0 & 0 & 0 & \xi_C & \eta_C & 1 & -Y_C\xi_C & -Y_C\eta_C \\ \xi_D & \eta_D & 1 & 0 & 0 & 0 & -X_D\xi_D & -X_D\eta_D \\ 0 & 0 & 0 & \xi_D & \eta_D & 1 & -Y_D\xi_D & -Y_D\eta_D \end{pmatrix} \cdot \begin{pmatrix} a_1 \\ a_2 \\ a_3 \\ b_1 \\ b_2 \\ b_3 \\ c_1 \\ c_2 \end{pmatrix} = \begin{pmatrix} X_A \\ Y_A \\ X_B \\ Y_B \\ X_C \\ Y_C \\ X_D \\ Y_D \end{pmatrix} \tag{11}$$

The solution of the equation system is given by the vector containing the 8 parameters a1 to c2, so that all other real-world coordinates $\tilde{X}, \tilde{Y}$ of the image can be calculated using the equations (7) and (8). The associated pixel positions $\tilde{\xi}, \tilde{\eta}$ do not match to the discrete pattern on the chip necessarily. In this case, FMAS conducts a bi-linear interpolation to calculate the discrete coordinates. Figure 5 shows the coordinates for $\hat{x}$ within the $\tilde{\xi}, \tilde{\eta}$-system that do not exactly fit into the pixel pattern (blue dots) because they are not integers. Equation (12) describes how the bi-linear interpolation method is used to calculate discrete coordinates considering the weight of the distances h, v, (1-h) and (1-v) to the surrounding pixels.

$$\begin{aligned} \mathrm{GW}(\tilde{\xi}_i, \tilde{\eta}_j) = {} & \mathrm{h} \cdot \mathrm{v} \cdot \mathrm{GW}(\xi_m, \eta_n) + (1-\mathrm{h}) \cdot \mathrm{v} \cdot \mathrm{GW}(\xi_m, \eta_{n+1}) + \mathrm{h} \cdot (1-\mathrm{v}) \cdot \mathrm{GW}(\xi_{m+1}, \eta_n) \\ & + (1-\mathrm{h}) \cdot (1-\mathrm{v}) \cdot \mathrm{GW}(\xi_{m+1}, \eta_{n+1}) \end{aligned} \tag{12}$$

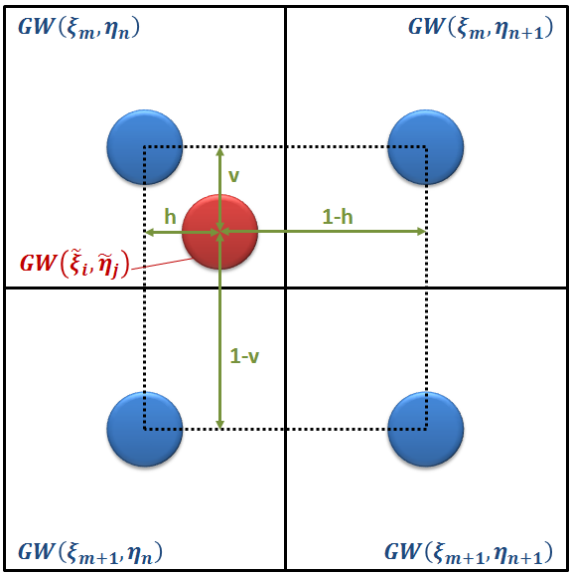

FIGURE 5. Bi-linear interpolation [5]

The image rectification is the last correction algorithm that is applied to the raw image. It is followed be the extraction of power and flux density information. All pixels outside the rectangle given by the rectified pass points are eliminated. The cropped image is saved as measurement image on the hard disk.

The power Φ distributed on the target and on the aperture is calculated by scaling the corresponding totalized flux density values with the surface area of one pixel (see equations (13) and (14)).

$$\Phi_{Target} = \frac{A_T}{\xi_{max,T} \cdot \eta_{max,T}} \cdot Gain \cdot \sum GW_T \tag{13}$$

$$\Phi_{Apertur} = \frac{A_A}{\xi_{max,A} \cdot \eta_{max,A}} \cdot Gain \cdot \sum GW_A \tag{14}$$

The flux density E distributed on the target and on the aperture is calculated by dividing the power by the correlated area in real-world coordinates (see equations (15) and (16)).

$$E_{Target} = \frac{\Phi_{Target}}{A_{Target}} \tag{15}$$

$$E_{Apertur} = \frac{\Phi_{Apertur}}{A_{Apertur}} \tag{16}$$

The last result to be calculated from the corrected measurement image is the position of the center of gravity of the flux distribution on the target. Its coordinates are calculated using the moments M_ξ and M_η around the ξ-axis and the η-axis. This calculation is mathematically similar to the calculation of a center of mass, in which the sum of a body's mass points is composed. The image moments use the sum of all gray values $GW(i,j)$ instead (see equations (17) to (19)).

$$\{\bar{\xi}, \bar{\eta}\} = \left\{\frac{M_\xi}{\sum GW}, \frac{M_\eta}{\sum GW}\right\} \tag{17}$$

$$M_\xi = \sum_{i=0}^{(\xi_{max,T})-1} \sum_{j=0}^{(\eta_{max,T})-1} GW(i,j) \cdot i \tag{18}$$

$$M_\eta = \sum_{i=0}^{(\xi_{max,T})-1} \sum_{j=0}^{(\eta_{max,T})-1} GW(i,j) \cdot j \tag{19}$$

VALIDATION

The software testing of FMAS is conducted at the Solar Furnace and High Flux Solar Simulator at DLR. Figure 6 illustrates the three main steps building a complete measurement sequence. The camera and the radiation source are fixed. The target is moved by a 3-axis-table after reading the sensor value.

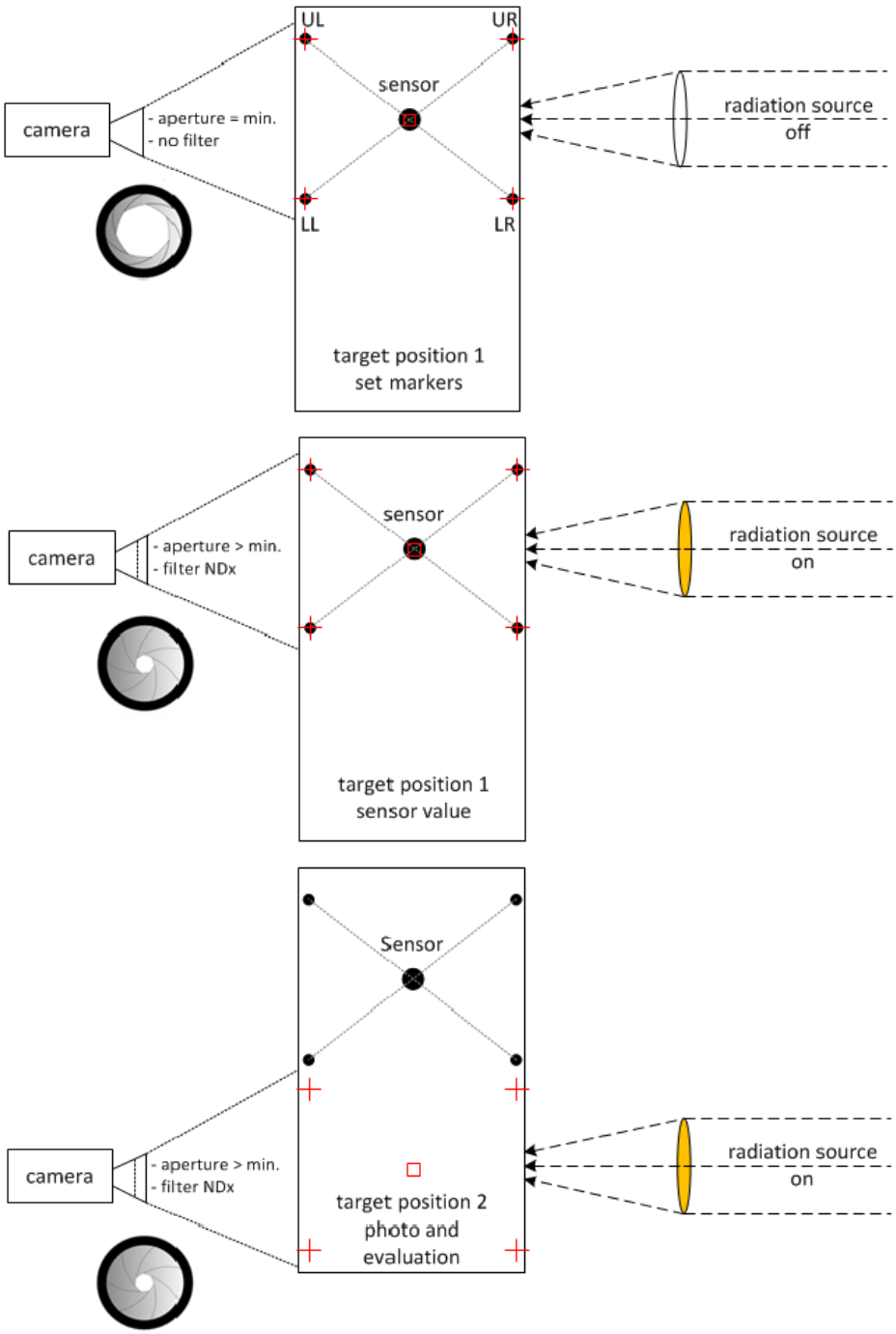

FIGURE 6. Measurement sequence

DLR High Flux Solar Simulator HLS

The tests carried out at the *HLS* are described in this section.

Figure 7 illustrates the main components of one xenon lamp arrangement. There are ten of those lamps available in the *HLS* in Cologne [5].

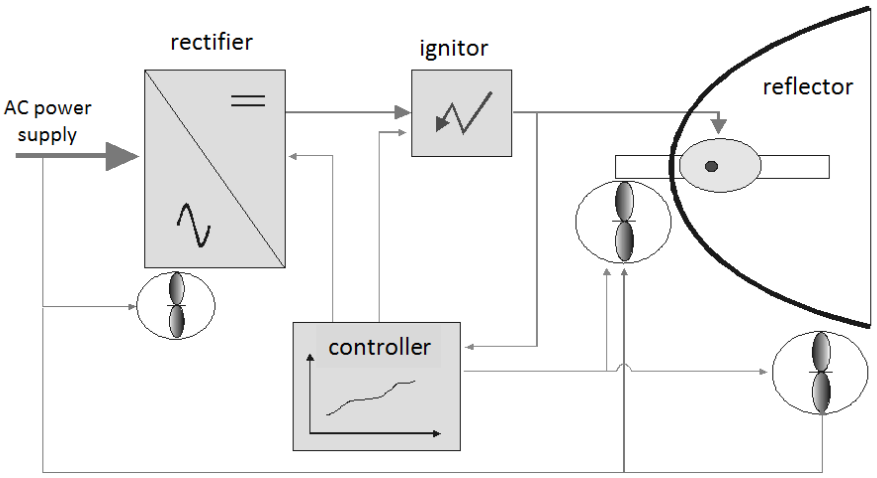

FIGURE 7. Block diagram of the HLS emitter [5]

The optical power is calculated by the following equations (20) to (22). The given efficiency factors are taken from manufacturer's specifications so that the calculated power values represent theoretical data and are used to quantifying deviations to *FMAS*.

$$\Phi = P_{el} \cdot \eta_{rectifier} \cdot \eta_{lamp} \cdot \eta_{reflectance} \cdot \eta_{spilling} \tag{20}$$

$$\Phi_{6000} = 6\,\text{kW} \cdot 0{,}9 \cdot 0{,}5 \cdot 0{,}9 \cdot 0{,}85 = 2{,}07\ kW \tag{21}$$

$$\Phi_{7000} = 7\,\text{kW} \cdot 0{,}9 \cdot 0{,}5 \cdot 0{,}9 \cdot 0{,}85 = 2{,}41\ kW \tag{22}$$

with P describing the electrical power and η the corresponding efficiencies. The ten reflectors of the HLS are assembled with both 7-kW-lamps and 6-kW-lamps that are used in parallel during the measurements. Figure 8 contrasts the calculated power data with the measured values on the basis of five independent measurement cycles.

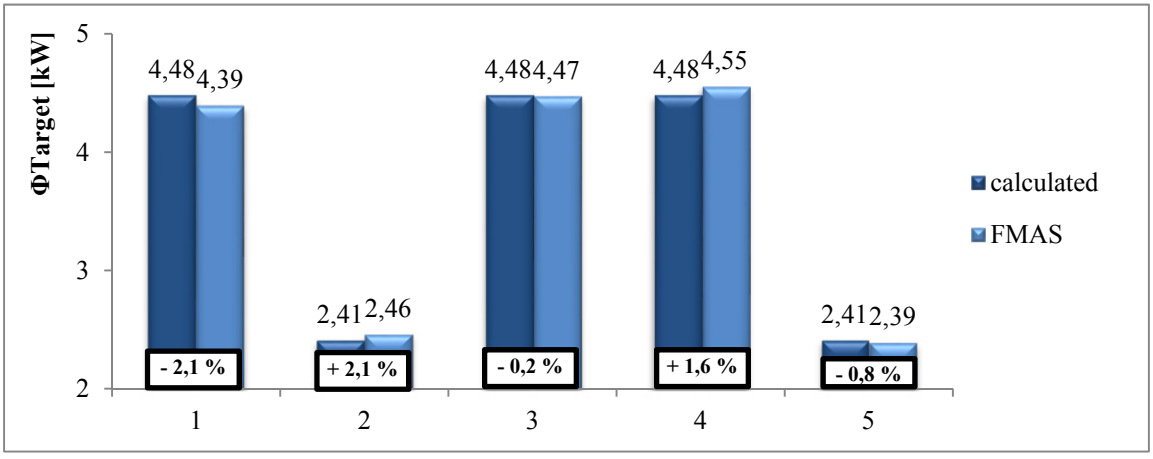

FIGURE 8. Calculated and measured flux (HLS) in 5 independent test cycles

The absolute deviation averages out at 1.4 %. The maximum accuracy, when using a Gardon radiometer with an accuracy of ±0.7%, adds up to ± 2.8 %.

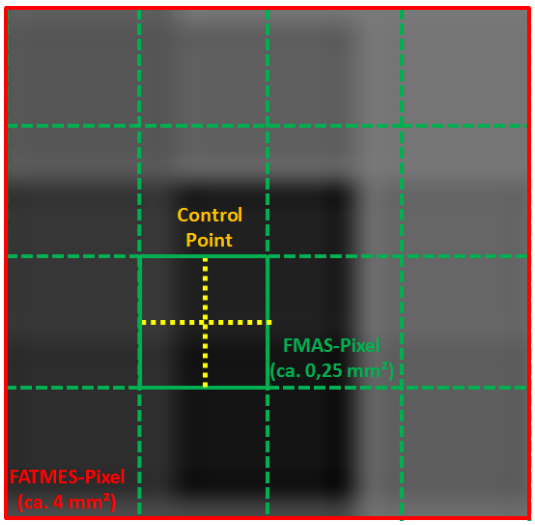

FIGURE 9. Comparison of image resolution

If the pass points defining the target area are conscientiously marked onto the image, there will nevertheless emerge an inaccuracy of about 3 % from the calculation of the surface and with it of the evaluated radiation flux (power). Assuming a target width and height of 200 mm, FATMES can, due to the lower resolution, determine a target area of 41,209 mm² at maximum, FMAS on the other hand gives 40,000 mm², which is a deviation of about 3% (see Fig. 9). The same occurs for the aperture, correspondingly.

Furthermore, a lower accuracy by reason of the image rectification is supposed. To identify the influence of the rectification calculation, comparing measurements with an integrating sphere are conducted. It appears that the nontransparent rectification algorithm of *FATMES* cause up to 2.8 % error while *FMAS,* with a deviation of 0.4%, can be assumed uninfluential (see Fig. 10).

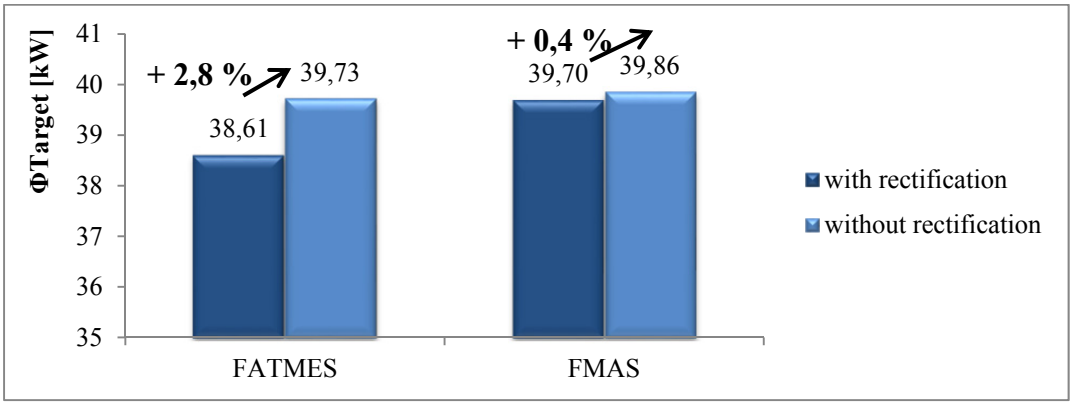

FIGURE 10. Effect of image rectification

During the development process of *FMAS* the use of a median filter was planned to be implemented (see Fig. 6). The former *FATMES* applies a linear filter to the image before the rectification. Figure 11 illustrates the reason why *FMAS* no longer requires any kind of gray-value-changing filter. Its raw resolution is high enough to represent the shape of the flux distribution. The use of a median filter during the test phase led to smaller values than calculated and expected. Without any filter algorithm the results were mostly precise.

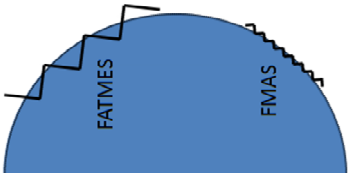

FIGURE 11. Resolution at edges

RESULT

The newly developed flux map acquisition system displays a good reproducibility and a low error (3%) in acquiring power data in the field of concentrated solar applications, i.e. solar towers. Its algorithms are documented ([9]), comprehensible and fast; the hardware is standard personal computer equipment with a commercial photogrammetry camera, thus easy to transport and widely deployable. Further applications outside of the field of concentrated solar power are possible, i.e. in every application where a measurement of photometric brightness is necessary or desirable.

TABLE 1. Comparison of measurement systems

feature	FATMES	FMAS
resolution	2 mm per pixel	0.5 mm per pixel
portability	localized	mobile
performance	3 minutes per evaluation	3 seconds per evaluation
data	display only	portable (bmp, csv)
technology	VAX (1977)	Windows computer
camera interfaces	BNC / Chinch	GigE / Ethernet
user interface	keyboard only	mouse and keyboard
algorithms	nontransparent	self-implemented
accuracy	> 5 %	< 3 %

REFERENCES

1. R. Gardon, "An Instrument for Direct Measurement of Intense Thermal Radiation," *The Review of Scientific Instruments (Volume 24, Number 5),* pp. 366-370, Mai 1953.
2. J. M. Kendall, Sr. and C. M. Berdahl, "Two Blackbody Radiometers of High Accuracy (Vol. 9, No. 5)," *Applied Optics,* pp. 1082-1091, Mai 1970.R. T. Wang, "Title of Chapter," in *Classic Physiques*, edited by R. B. Hamil (Publisher Name, Publisher City, 1999), pp. 212–213.
3. U. Groer and A. Neumann, "Development and testing of a high flux calorimeter at DLR Cologne," *Journal de Physique IV (STCT 9),* pp. 643-648, 1999.B. R. Jackson and T. Pitman, U.S. Patent No. 6,345,224 (8 July 2004)
4. J. Kaluza, A. Neumann "Comparative Measurements of Different Solar Flux Gauge Types," *ASME Journal of Solar Energy Engineering, vol. 123,* vol. 123.
5. Ferriere, A., Robert, J.-F., Kaluza, J., and Neumann, A., 2000, ''Concentrated Solar Flux Measurements: Results of the Second SolarPACES Fluxmeter Intercomparison Campaign,'' Proc. 10th SolarPACES Int. Symp. on Solar Thermal Concentrating Technologies, Sydney, Australia.
6. Ballestrín, J., M. Rodrıguez-Alonso, J. Rodrıguez, I. Canadas, F. J. Barbero, L. W. Langley, and A. Barnes, "Calibration of high-heat-flux sensors in a solar furnace", Metrologia 43 (2006) 495–500.
7. G. Heising, Skript zur Vorlesung Digitale Videotechnik - Bildverarbeitung 2, TFH Berlin, 2002.
8. G. Dibowski, "Betriebshandbuch Hochleistungsstrahler", Deutsches Zentrum für Luft- und Raumfahrt e. V., 2011.
9. M. Thelen, "Entwicklung eines optischen Messsystems für Strahlungsflussdichteverteilung und Verifizierung anhand hochkonzentrierter Solarstrahlung", Master Thesis, Deutsches Zentrum für Luft- und Raumfahrt e. V., 2016.